

# Photoluminescence for Defect Detection on Full-Sized Photovoltaic Modules

Bernd Doll<sup>ID</sup>, Johannes Hepp<sup>ID</sup>, Mathis Hoffmann<sup>ID</sup>, René Schüler, Claudia Buerhop-Lutz<sup>ID</sup>, Ian Marius Peters<sup>ID</sup>, Jens A. Hauch, Andreas Maier<sup>ID</sup>, and Christoph J. Brabec

**Abstract**—Cost-effective, fast, and nondestructive on-site characterization of photovoltaic plants is required to determine countermeasures against power loss, defects, or safety problems. Methods with small impact on the operation and a high throughput, such as infrared thermography (IR), or methods with high resolution for detailed defect information, such as electroluminescence (EL) imaging, are expedient. To combine high resolution and high throughput, we propose to use photoluminescence (PL) as an outdoor characterization method for full-sized module imaging. With PL imaging as with IR imaging, no electrical contact is necessary, yet image resolution is on par with EL images. Our outdoor PL setup features an excitation source with 18 broadband, white, high power, chip on board LEDs coupled with low-cost short pass filters. This setup is suitable for indium gallium arsenide and silicon detectors. Here, we compare the visibility of common defects, including short-circuited bypass diodes, cracks, potential induced degradation, snail trails, ethylene-vinyl acetate degradation, and

interconnection failures, in PL images to that in state-of-the-art imaging techniques IR, EL, and ultraviolet fluorescence. We find that out of these seven defects, five can be detected well, cell cracks under certain conditions, and interconnection failures not at all. We discuss how different techniques are complementary to enable better defect detection.

**Index Terms**—Defect detection, fluorescence, luminescence, photoluminescence, photovoltaic (PV) systems, silicon (Si).

## I. INTRODUCTION

POTOVOLTAIC (PV) plants are assessed on-site for commissioning, to determine the cause of power loss observed in monitoring data, to avoid safety issues, and to determine the best future operation and maintenance (O&M) strategy [1], [2].

Ideal O&M strategies consider the likely occurrence of future defects. Defect formation depends on PV module architecture and module stress during operation. One study showed that, on average, more than one defect-generating weather event occurs within ten years [3]. Hence, PV systems from the major installation years 2010 to 2012 in Germany [4], accounting for 23 GW [5], are likely to have weather-induced defects by now. This suspicion is supported by infrared (IR) thermography imaging studies, which showed that over 86% of the inspected PV plants have deficiencies [6] of various kinds. Yet, nature and severity of these defects are often unknown, and whether and when there is a need for maintenance is unclear.

IR imaging is the most commonly used tool for outdoor PV-module analysis. It allows identifying faulty modules without any disruption of PV plant operation. Outdoor IR detector resolution is typical below  $640 \times 480$  pixels, but due to uniform heat dissipation between the semiconductor and the glass front side, higher resolution would not bring advantages [7]. IR imaging is also limited to defect types that are thermally active at the time of measurement. Such defects need strings or modules not to operating at maximum power. Deviation from maximum power can be caused by various defects, such as a defective bypass diodes, potential induced degradation (PID), or hot-spots [8]–[12]. Additionally, IR imaging is limited with respect to the conditions under which measurements are possible. Ideal measurement conditions, according to the “IEA-PVPS T13-10:2018” report [7], are an irradiance above  $700 \text{ W/m}^2$  on a cloud free day.

A more profound investigation of deficiencies occurring in a PV-installation require additional characterization [13]. A variety of nondestructive characterization methods exists in the

Manuscript received March 29, 2021; revised June 5, 2021; accepted July 19, 2021. Date of publication August 23, 2021; date of current version October 21, 2021. This work was supported in part by the German Federal Ministry for Economic Affairs and Energy (BMWi) Project iPV4.0 (FKZ: 0324286) and Project COSIMA (FKZ: 032429A), in part by the IBC SOLAR AG Project iPV4.0 (FKZ: 0324286), and in part by the State of Bavaria via the Project PV-Tera (446521a/20/5). (Corresponding authors: Bernd Doll; Ian Marius Peters.)

Bernd Doll and Johannes Hepp are with the Faculty of Engineering, Materials for Electronics and Energy Technology and Graduate School in Advanced Optical Technologies, Friedrich-Alexander University Erlangen-Nürnberg, 91054 Erlangen, Germany, and also with the High Throughput Methods in Photovoltaics, Forschungszentrum Jülich GmbH, Helmholtz Institute Erlangen-Nürnberg for Renewable Energy, 90429 Erlangen, Germany (e-mail: bernd.doll@fau.de; johannes.hepp@fau.de).

Mathis Hoffmann is with the Faculty of Engineering, Materials for Electronics and Energy Technology and Pattern Recognition Lab, Friedrich-Alexander University Erlangen-Nürnberg, 91054 Erlangen, Germany (e-mail: mathis.hoffmann@fau.de).

René Schüler is with IBC SOLAR AG, Bad Staffelstein 96231, Germany (e-mail: rene.schueler@ibc-solar.de).

Claudia Buerhop-Lutz, Ian Marius Peters, and Jens A. Hauch are with the High Throughput Methods in Photovoltaics, Forschungszentrum Jülich GmbH, Helmholtz Institute Erlangen-Nürnberg for Renewable Energy, 90429 Erlangen, Germany (e-mail: c.buerhop-lutz@fz-juelich.de; i.peters@fz-juelich.de; j.hauch@fz-juelich.de).

Andreas Maier is with the Pattern Recognition Lab, Erlangen, Friedrich-Alexander University Erlangen-Nürnberg, 91054 Erlangen, Germany (e-mail: andreas.maier@fau.de).

Christoph J. Brabec is with the Faculty of Engineering, Materials for Electronics and Energy Technology, Friedrich-Alexander University Erlangen-Nürnberg, 91054 Erlangen, Germany, with the Bavarian Centre for Applied Energy Research, Erlangen, Germany, and also with the High Throughput Methods in Photovoltaics, Forschungszentrum Jülich GmbH, Helmholtz Institute Erlangen-Nürnberg for Renewable Energy, 90429 Erlangen, Germany (e-mail: christoph.brabec@fau.de).

Color versions of one or more figures in this article are available at <https://doi.org/10.1109/JPHOTOV.2021.3099739>.

Digital Object Identifier 10.1109/JPHOTOV.2021.3099739

lab, and it has been shown that combining several methods to detect more defect types is expedient [7]. Yet, many of these tools are used as inline inspection tools at different production steps in the semiconductor production lines [14], [15], but not as mobile tools in the field. Utility of these methods for defect detection and analysis motivated the development of a tool to complement IR imaging that is capable of outdoor usage and high throughput.

Among the suitable tools are automated optical inspection (AOI) methods, which detect different defects under repeatable indoor conditions. Visual inspection, thermography, electroluminescence imaging (EL) and photoluminescence (PL) imaging are used to determine cell properties and defects in the earliest stages of production, using conventional analysis [16] or deep learning [17]. These AOI methods help to maintain and improve cell efficiencies, and to determine possible production improvements by automated detection of defects like microcracks [18].

Luminescence imaging is especially promising since it has a principally higher spatial resolution than IR imaging. Current tools have resolution of up to  $2000 \times 2000$  pixels, depending on the used camera, which allows a more detailed defect determination [19] than IR imaging. An overview of common defects is given in the international standard “IEC TS 60904-13” [20]. Among them are cell defects such as cracks, wafer contaminations, soldering or ribbon interconnection failures, and chemical corrosion (snail trails). Also visible are module defects like PID, cell mismatch and short-circuited bypass diodes. Importantly, luminescent methods work best at night when the PV system is offline.

In luminescent imaging, two techniques are distinguished by source of excitation. In EL, carriers are excited through an external power source, in PL through illumination. Either technique allows controlling light emission from the module by changing the intensity of excitation [21]. The main disadvantage of state-of-the-art EL is the need for electrical contacts [22]. PL, on the other hand, is used without the need to access the circuitry. To turn PL into a high throughput method for field measurements, several challenges must be overcome.

Up to now, PL has been established in the lab for cell and module measurements [23]–[25]. Only few concepts for PL in the field exist. One example of a night-time technique is 2-D excitation by a laser [26]. Yet, this method is currently not capable of measuring a large number of modules in a short time.

To turn PL into a high throughput method, a suitable artificial light source is needed. Due to the high lateral diffusion inside a single silicon (Si) solar cell, the emitted PL intensity level is quite homogeneous and cell defects can be detected easily [23]. The luminescence intensity of different cells is determined by the minority charge carrier concentration generated by the excitation source [27]. Thus, the excitation homogeneity of the artificial light source plays an important role for proper defect detection in PL, especially on the module scale.

Researchers from the University of New South Wales [28], [29] and from Technical University of Denmark [26], [30] are working on PL tools with 2-D excitation laser line scanning. Published images show promising results. Compared to the setup, we introduce here, higher intensities can be reached and the excitation orientation can be changed. Thus, different working

points of the modules can be set and additional information can be extracted [31]. With a partial excitation of the 2-D laser post processing is necessary to achieve 2-D images. This method looks good, but real outdoor PL images have not yet been achieved.

In addition to these tools, daylight applications using sunlight as excitation source are published. Alternatively, substrings are modulated with a cell-sized illuminated cover [32], [33] or via electrical circuit [34]. The PL images need to be calculated from an image sequence with a repetitive electrical modulation of the PV modules to minimize the sun’s background noise. Except for the cell-sized illumination cover, which requires one image sequence per bypass diode, all methods interrupt operation due to the electrical contacts. With our setup PV modules without operation disruption can be captured with a single PL image.

In this article, we aim to establish full area PL video imaging as a technique for high throughput characterization of faulty modules in the field. We use an in-house developed mobile PL measurement setup for characterization, and compare the detectability of defects for this tool with that of other imaging techniques (EL, IR, ultraviolet fluorescence (UV-F)). Up to date, our method is, to the best of authors’ knowledge, the only PL technique to provide full PV module images recorded outdoors with an artificial light source at night. We show qualitatively and quantitatively which defect types can be identified, and which cannot. To explore specific defect types, we use modules with known defects and make a side-by-side comparison of the resulting images taken with the different techniques. We find that out of seven common selected defects, PL can identify five with certainty: short-circuited bypass diodes, cell cracks, PID, snail trails and ethylene-vinyl acetate (EVA) degradation, and one—inactive areas—under suitable conditions. Interconnection failures are not detectable, due to the excitation character of PL.

## II. EXPERIMENTAL DETAILS

### A. Experimental Setup and Discussion of Light Homogeneity

Our PL setup consists of an excitation unit (light source) and a camera unit. The excitation unit allows full area illumination of the PV modules with an area of about  $2 \text{ m}^2$ . A total of 18 low-weight chip-on-board LED modules are used. A high homogeneity level can be achieved by adjusting angle and intensity of the single LED-modules.

The camera unit is suitable for EL and PL images. Indoor PL images shown in this publication were all recorded with the front illuminated Si charge-coupled device camera GE FI 2048 2048 from greateyes GmbH from Germany with a resolution of  $2048 \times 2048$  pixels. The outdoor PL images shown in this publication were all recorded with indium gallium arsenide (InGaAs) cameras, namely a Ninox 640 or Owl 1280 from Raptor Photonics Limited from Northern Ireland. Additionally, movie recording with these InGaAs cameras is possible, as was presented in a previous publication [22]. Comparison of different cameras is discussed in [35]. Short pass filters KG5 from Schott AG from Germany with a cut-off wavelength of 800 nm are used in front of each LED module, and a custom-made long pass filter with a cut-on wavelength of 970 nm in front of the camera. With

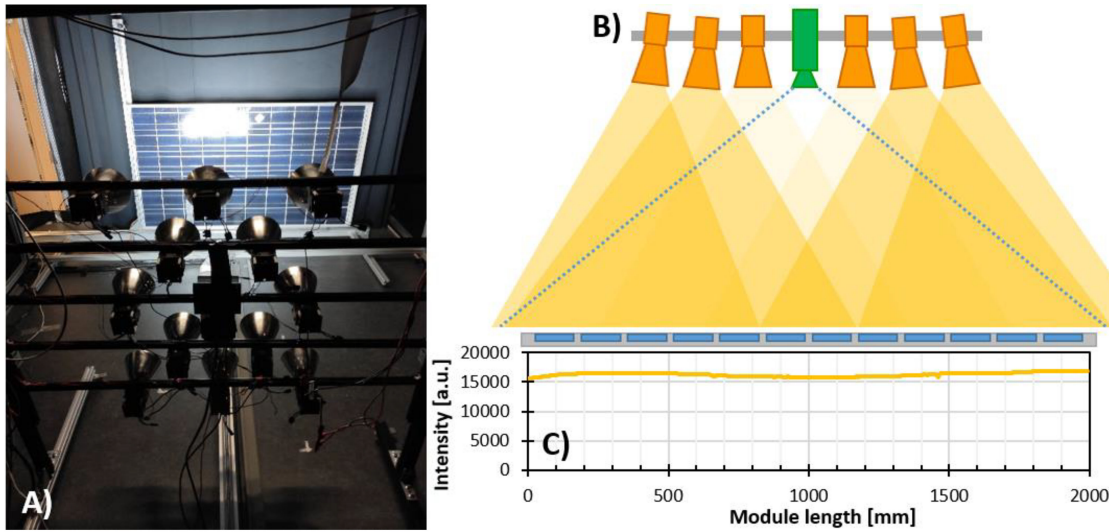


Fig. 1. (a) View of the indoor PL setup from the back to excitation direction. (b) Schematic sketch of the LED-module alignment and intensity adjustments, with the corresponding homogeneity line scan (c) across a 72 Si cell module area. The homogeneity was measured with three phosphorous cardboards. At 650 mm and 1450 mm small spikes between the cartons can be seen.

both filters, excitation light is suppressed and it cannot reach the camera's detector.

For outdoor applications, excitation unit and camera unit are mounted on a prototype tilting-cart. Moving this cart manually in front of a line of modules in an initial field test, we achieved a throughput of up to 37 PV modules per minute. For future implementation, a mobile power supply is in development.

The unequivocal identification of several defects requires a high level of homogeneity in illumination. To achieve this, we included the possibility for two adjustments in our LED modules. Direction and intensity of the light cones can be adjusted individually for each LED module [sketched schematically in Fig. 1(b)]. By combining these adjustments, high light intensities in the module center are avoided. Fig. 1(c) shows the intensity in the center of the module position from an image of a phosphorous cardboard. The phosphorous cardboard is necessary to surpass the PL filter system and gives a high resolution of the excitation distribution. The mean excitation intensity in the sample is 37 W/m<sup>2</sup> with a standard deviation of about 3.8 W/m<sup>2</sup> measured with an irradiance sensor at nine different positions.

This level of homogeneity is sufficient to identify module level defects, such as PID. A detailed explanation for PID detectability and the reliability to high excitation homogeneity levels is given in Section III-A. Intensity variations are no issue for detecting cell-level defects, as within a cell the PL signal intensity is very homogeneous, and abnormalities like cracks and inactive areas can easily be identified [22] (see Section III-B). The detectability of defects in the electrical connection between cells and modules is discussed in Section III-C.

#### B. PL Intensity and PL Ratio

In quasi-steady-state PL (QSS-PL), the luminescence intensity is determined by the minority charge carrier density. PL differs from EL in that the luminescence intensity is generated by the injection of majority charge carriers and the generation of excess minority charge carriers at the pn junction [25]. Thus, the

QSS-PL intensity  $I_{PL}$  depends on the spatially averaged excess minority carrier concentration [36]. With a variation of the excitation intensity, a pseudo  $I$ - $V$  curve is obtained. The implicit voltage required for this is determined from the quasi-Fermi level splitting [36]

$$I_{PL} = A \cdot B \cdot n_i^2 \cdot \exp\left(\frac{\Delta\eta}{kT}\right); \Delta\eta = eV \quad (1)$$

with  $A$  is a calibration factor,  $B$  is the radiative recombination coefficient,  $n_i$  is the intrinsic carrier concentration, and  $\Delta\eta$  is the quasi-Fermi level energy separation. Due to the large lateral diffusion of the charge carriers in Si [23], each PV cell emits an almost homogeneous PL intensity, depending on the excitation intensity for this cell and independent of the excitation distribution within the cell.

With different excitation levels of the semiconductor, additional information about the visible defects can be extracted. Areas of low emission intensity in EL and high emission intensity in PL are indicative of increased series resistance to neighboring regions. Dark regions in both luminescence techniques indicate poor quality of the semiconductor material and increased non-radiative recombination [25], [37].

Two heuristic factors,  $A$  and  $B$ , were used in the previous equation. Both are influenced by camera, semiconductor, and optical properties. All influences make quantification difficult in the laboratory [38]. In the field, where excitation homogeneity and camera positions are not reproducible, a simpler method for quantifying PL data is needed. The intensity ratio  $I_{H/L}$  of each pixel for two images at different excitation intensities, high and low, is such a simple approach, and the relationship can be reduced to

$$I_{H/L}(A, B) = \frac{I_{PL, High}(A, B_{High})}{I_{PL, Low}(A, B_{Low})}. \quad (2)$$

The calibration factor  $A$  is constant for identical camera parameters so that additional information of the radiative recombination can be extracted. The intensity differences visible in the

image are due to different excess minority carrier concentration and small changes of radiative recombination coefficient  $B$  for the range of high (about 30 W/m<sup>2</sup>) and low (about 10 W/m<sup>2</sup>) excitation intensity. Equations (1) and (2) lead to

$$I_{H/L} = C \frac{B_{\text{High}}}{B_{\text{Low}}} \frac{e}{kT} [\Delta\eta_{\text{High}} - \Delta\eta_{\text{Low}}] \quad (3)$$

where  $C$  is a constant correction factor. Hence, the difference in luminescence intensity is mainly due to the difference in quasi-Fermi level splitting. In particular, areas with a high PL ratio, indicating of a reduced parallel resistance with a very high sensitivity. Thus, PID can be detected at a very early stage. Values smaller than the increase of the excitation level ratio are indicative of a strongly reduced parallel resistance.

### C. Other Outdoor Imaging Techniques and Measurement Conditions

To benchmark the utility of PL images for defect detection and identification, we compared them with different state of the art outdoor imaging techniques, including IR, EL, and UV-F imaging. The latter is a technique to analyze EVA degradation, which was used together with visual inspection. In this section, we shortly describe the measurement details and classify the repeatability for each technique.

**1) EL Imaging:** EL imaging is the recording of light emitted by radiative recombination of free charge carriers after excitation with charge carrier injection at the electrodes and using an external voltage source. It was first published for PV applications in 2005 [19].

EL intensity distribution provides detailed information of the semiconductor and electrical circuit properties and allows, for example, series resistance mapping [39] and crack detection [40].

Here, the following two modalities were used: one with low injection current (10% of short-circuit current  $J_{SC}$ ) and one with high injection current, (90% of  $J_{SC}$ ). Those different modalities were applied to investigate the influences of parallel and series resistances. Series resistance increasing defects, such as inactive areas, are easier detected at high injection currents, and parallel resistance decreasing defects at low injection currents. Camera settings of the GE FI 2048 2048 for EL were an integration time of 15 s, an aperture of 2.8, and detector cooling was set to a temperature of  $-10^{\circ}\text{C}$ .

For indirect semiconductors, such as Si, during EL imaging, excitation and luminescence intensity are influenced by temperature [35]. This influence is small compared to that of intensity and homogeneity variations in PL. For indoor EL, AOI defect detection algorithms exist and are commonly used [17], [41]. Additionally, other module properties, such as module power, can also be predicted [42].

**2) PL Imaging:** PL images were recorded with either our indoor or our outdoor setup. Indoor PL images at different excitation levels were acquired with a mean irradiance of 36.4 W/m<sup>2</sup> and a standard deviation of 3.8 W/m<sup>2</sup>, measured with a standard Si irradiance sensor. The distance between camera and LEDs to the PV modules was 385 cm. Camera settings for the GE FI 2048 2048 indoor measurements were an integration time of 30 s, an

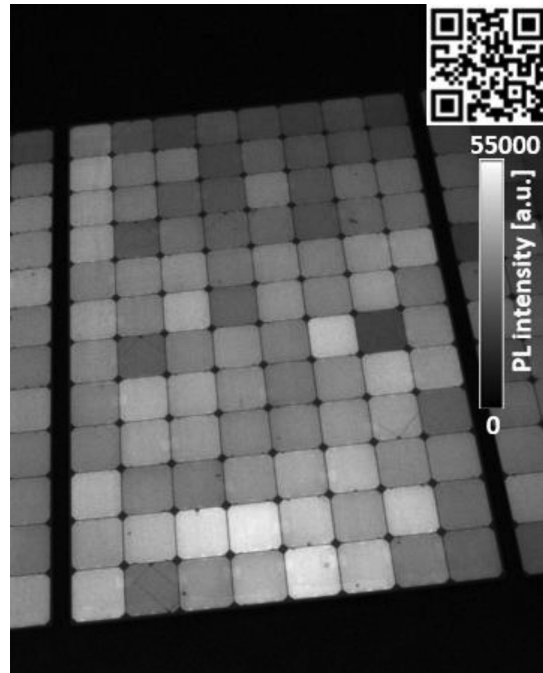


Fig. 2. Screenshot of PV module #4 of the PL video recorded outdoors in the field linked to with the QR-Code in the corner. The PL video shows real time speed.

aperture of 2.8, and detector cooling was set to  $-10^{\circ}\text{C}$ . PL ratio images were calculated from the two images with different excitation.

PL images outdoors were taken with the Ninox 640 camera, at an excitation irradiance of 142 W/m<sup>2</sup>, a distance between camera and LEDs to the PV modules of 300 cm to 340 cm, an integration time of 5 ms, an aperture of 1.4, and detector cooling set to  $0^{\circ}\text{C}$ .

The homogeneity of Si cell excitation is influenced by the camera/LED to PV module distance and angle, which are nearly impossible to reproduce outdoors. First tries to analyze the PL image quality has been done by Trupke *et al.* [33] for daylight PL. Finally, PL has a lower repeatability compared to EL, but qualitative defect recognition is repeatable.

Automated defect detection algorithms are not available for module sized PL images. However, many of the state-of-the-art AOI methods rely on data-driven learning. We are confident that these can be transferred to PL, given an appropriate training data set, similar to our implication of PL power prediction [43].

**3) Video PL Imaging:** PL movies outdoors were taken with the Owl 1280 camera at an excitation irradiance of about 140 W/m<sup>2</sup>, a distance between camera and LEDs to PV modules of 300 cm to 400 cm, an integration time of 5 ms, an aperture of 1.4, and detector temperature set to  $0^{\circ}\text{C}$ . With this camera setting, video recording without further camera stabilization and low motion blur is possible.

The QR-Code in Fig. 2 leads to an uploaded PL video taken with the mentioned parameters under outdoor conditions. The PL image of Fig. 2 is a screenshot of PV module #4 of that video.

**4) Thermography:** IR images were recorded using a hand-held setup. The PV modules were connected either to an external electrical load or to other modules in a PV string, and were monitored with an IR camera at our test facility in Erlangen. For

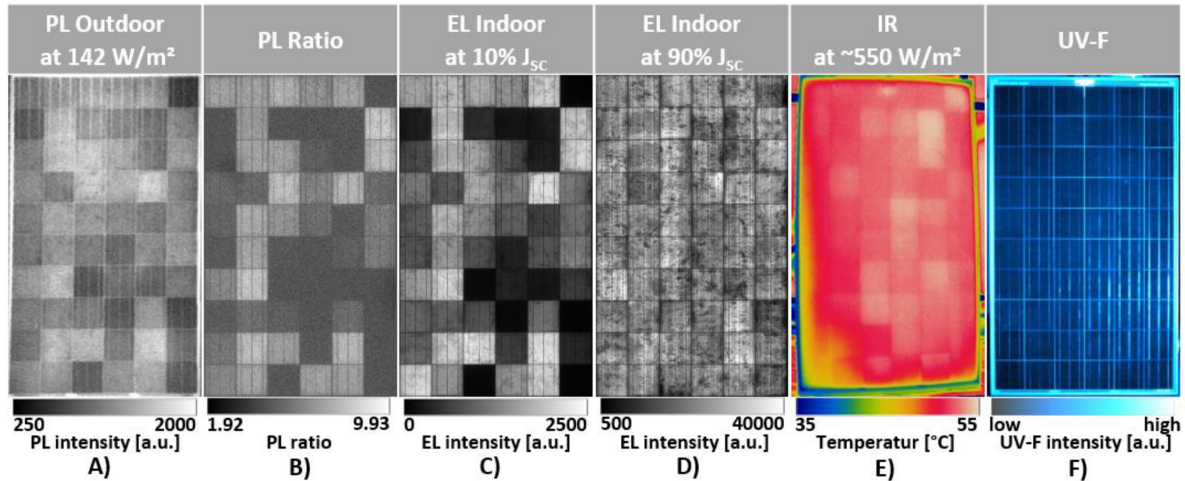


Fig. 3. Images of one PV module with PID for the different imaging techniques and conditions, namely: (a) PL outdoor with a mean excitation intensity of  $142 \text{ W/m}^2$ , (b) PL ratio, (c) EL indoor with a current of 10% of the  $J_{\text{SC}}$ , (d) EL indoor with a current of 90% of the  $J_{\text{SC}}$ , (e) IR at an irradiance of about  $550 \text{ W/m}^2$ , and (f) UV-F.

both setups, an Optris PI 450 camera from Optris GmbH was used with an integration time of 1 ms.

The repeatability of IR is affected by irradiance, ambient temperature, and wind cooling of the PV modules. All three parameters together are hardly reproducible, and IR signal evaluation is typically done via temperature differences [44]. Temperature differences are often reproducible and deep learning algorithms can be trained to detect defects [45].

5) *UV-Fluorescence Imaging*: UV-F imaging is the recording of fluorescence in the visible spectrum of the encapsulant material EVA after UV light excitation. This technique was first demonstrated by King *et al.* [46]. Fluorescence is mainly caused by chromophores, produced in the EVA by UV radiation and quenched by diffusing oxygen and water through the encapsulation polymers [47], [48].

Without cracks enabling oxygen and water diffusion through Si, only the gaps between cells are diffusion paths to the EVA. Thus, quenching begins at the cell edges, and the affected area grows inward with module age. Due to linear diffusion and quenching of the UV-F signal, different crack lifetimes can roughly be determined [49]. UV-F images in this article were acquired with a single UV excitation light source from MBJ and a commercial SLR camera, an *EOS 700D* from *Canon*, with an attached UV filter, an ISO value of 400, and an integration time of 5 s. UV-F as an inspection method is only useable after UV exposure in the field. Consequently, this technique is not used in production lines. Due to the visibility of the fluorescence EVA signal, the reproducibility of outdoor UV-F measurements is high and can easily be adjusted. AOI defect detection for an outdoor high throughput setup was recently presented by Gilleland *et al.* [50].

### III. COMPARISON OF DIFFERENT IMAGING TECHNIQUES FOR SELECTED DEFECTS

#### A. Potential Induced Degradation

PID is a defect formed by the potential difference between ground level and Si cells [51]. Due to the potential difference,

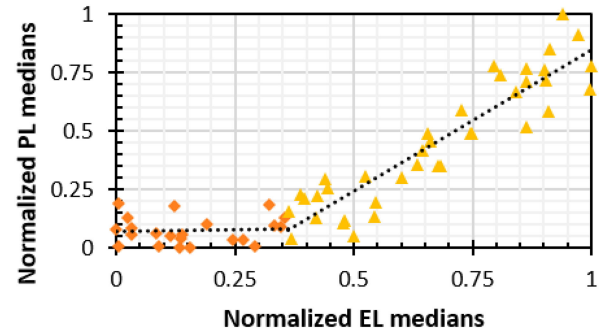


Fig. 4. Normalized median Intensities from indoor EL (10% of  $J_{\text{SC}}$ ) and PL (at  $37 \text{ W/m}^2$ ) images in relation. Threshold of dark cells in PL images for the data points below 0.33 are marked in orange. Yellow datapoints show direct linear dependency of luminescence intensity between PL and EL images.

ions migrate, aided by temperature and humidity. The inclusion of ions in the Si crystal structure leads to a change of recombination and parallel resistance (shunting) [52]. The typical PID pattern of a PV module consists of several affected cells appearing darker in EL images. This effect is especially visible in low intensity EL, PL, and PL ratio, and the typical chessboard like pattern is visible in Fig. 3(a)–(c).

Shunting causes power to dissipate through the parallel resistance, resulting in an additional heat source and temperature increase of the cell. PID is visible in IR images [see Fig. 3(e)], which was measured at an irradiance of approx.  $550 \text{ W/m}^2$ . PID is not visible in UV-F [see Fig. 3(f)], as it does not influence encapsulating polymers.

To quantify the detectability of PID in EL and PL, we plotted the median luminescence intensities after normalization of both images and plotted the corresponding values against each other in Fig. 4. Correlation is linear after a threshold in PL, marked orange. The threshold occurs due to the different charge injection levels used in EL and PL imaging. The yellow data points after the threshold indicate a direct linear dependency of luminescence intensity.

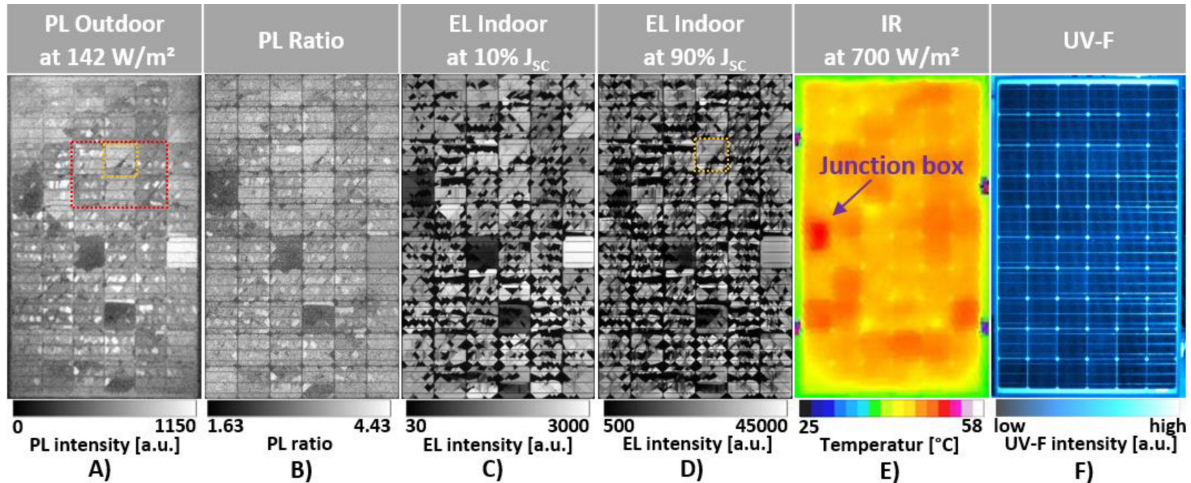


Fig. 5. (a) Images of one PV module with cracks and inactive areas for the different imaging techniques and conditions, namely: (a) PL outdoor with a mean excitation intensity of  $142 \text{ W/m}^2$ , (b) PL ratio, (c) EL indoor with a current of 10% of the  $J_{SC}$ , (d) EL indoor with a current of 90% of the  $J_{SC}$ , (e) IR at an irradiance of about  $700 \text{ W/m}^2$  with highlighted hit junction box, and (f) UV-F. Yellow marked cells in (a) and (d) are magnified in Fig. 6. Red marked cells in (a) are used for advanced imaging analysis for inactive area analysis.

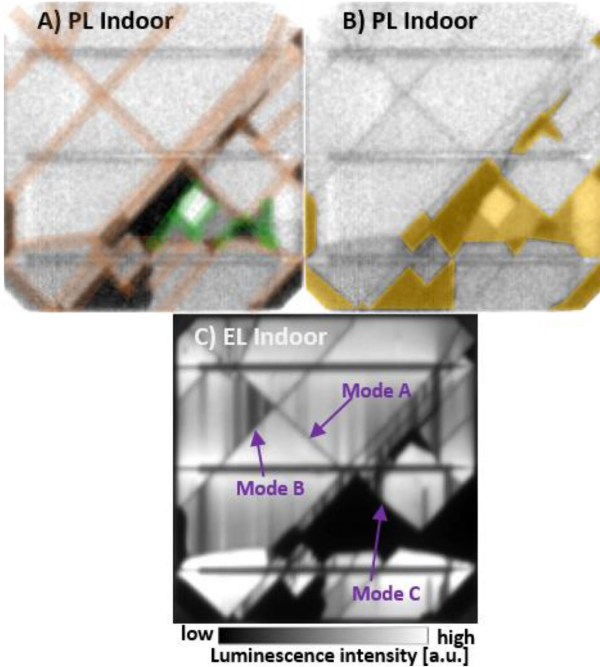


Fig. 6. Magnification of marked cell from Fig. 5. PL image in (a) with marked cracks, (b) with marked inactive areas and EL at 90% of  $J_{SC}$  (c) with marked cracks for the three different modes. Green marked cracks are only visible in PL because they are within an inactive/isolated area.

### B. Cracks

A crack appears when a Si wafer breaks, visible for all different imaging techniques in Fig. 5. Depending on the electrical connection to other parts of the wafer, cracks are classified into modes [7], [20]. We identify some examples in EL images shown in Fig. 6(c). Mode A cracks are electrically connected and appear as thin, dark lines in the luminescence images. Cracks in mode B are partially connected to their surrounding with a finite resistance. The luminescence of the enclosed area depends on this resistance. Mode C cracks are fully isolated, and enclosed areas appear black in EL images [see Fig. 6(c)].

In PL images, all electrically connected cell parts have roughly the same PL intensity, which is also the case for areas separated by mode A and mode B cracks, as is visible in Fig. 6(b). Areas separated by mode C cracks are completely disconnected and their PL intensity differs due to different recombination rates in the different cell parts. For sunlight excitation at high levels, presently not reachable with our outdoor setup, even mode B cracks are detectable [33]. Parameters influencing the recombination rates are local charge carrier lifetimes, the radiative recombination diode current, internal serial resistance, parallel resistance, and the local  $V_{OC}$ . Underlying physical defects may also shunt cell parts, and small differences in shunt resistance may have a strong influence on PL intensity. Differences in PL intensity are frequently observed, and isolated areas can be separated, as visible in Fig. 6(b) and (c). One exception exists: if recombination rates between two isolated areas do not differ, the PL intensity level of these two areas is similar and the isolated region is not detectable.

To give a quantitative comparison of crack detection in EL and PL, we manually counted the number of cracks. In Fig. 6(a) and (d), each detected crack is marked. Additional cracks inside the isolated area in the PL image are marked green. If only the orange marked cracks are counted, 39 were detected in each image.

For a quantitative analysis, we used thresholds to determine the inactive areas in EL and PL for six cells marked in Fig. 5(a). For EL, we used a threshold of 7000 counts, corresponding to approximately 15% of the highest luminescence intensities, and determined that 25.6% of the total area was inactive. For PL, a range of PL intensities has to be defined for working areas for each cell individually. We defined this range to be the difference between the mean minus 75% of the standard deviation and the mean plus 75% of the standard deviation. With these two thresholds, an inactive area of  $27.2\% \pm 6.3\%$  was obtained. The uncertainty can be reduced to 2.1% if an expert does the inactive area analysis manually. The determined inactive area is exemplary visible in Fig. 6(b) for one cell.

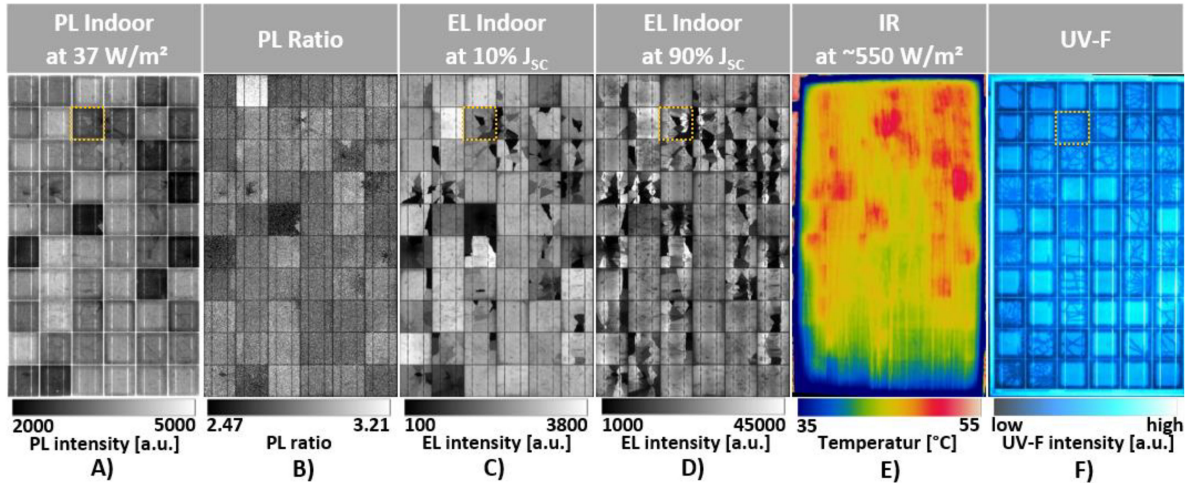


Fig. 7. (a) Images of one PV module with cracks and inactive areas for the different imaging techniques and conditions namely: (a) PL indoor with a mean excitation intensity of  $37 \text{ W/m}^2$ , (b) PL ratio, (c) EL indoor with a current of  $10\%$  of the  $J_{SC}$ , (d) EL indoor with a current of  $90\%$  of the  $J_{SC}$ , (e) IR at an irradiance of about  $550 \text{ W/m}^2$ , and (f) UV-F. Yellow marked cells in (a) and (d) are magnified in Fig. 8. Magnification of the PL [at  $37 \text{ W/m}^2$ , (b)], EL (at  $10\% J_{SC}$  in (c) and at  $90\% J_{SC}$ , (d) and the UV-F in (e)] with a highlighted younger crack, all of the same cell.

Thermally, modes A and B cracks cause very small energy losses and are typically not visible in IR images. Mode C cracks lead to a reduction of the active area leading to a reduction of the current generation of cells and energy consumption to achieve string level maximum power point currents. Depending on the disconnected area size, the cell temperature may increase due to the formation of a hotspot or the bypass diode becomes conductive. Similar behavior can also be observed for partial shading of the cell [20]. For a severely damaged PV module integrated within a PV string, as seen in Fig. 5(e), bypass diode conduction of all five substrings is visible in the IR image, indicated by a hot junction box. Consequently, the IR image does not show a unique, interpretable pattern.

The PV module in Fig. 5(f) does not show any UV-F signals even though cracks are present, due to the lack of UV light exposure in the field. In the following section, a module with cracks and UV light exposure and corresponding UV-F signature is discussed. UV-F is used to determine anomalies in EVA. An example of UV-F with optically activated EVA by UV light is shown in Fig. 7(f). Cracks in the Si layer open diffusion paths for oxygen and water vapor and thus result in EVA fluorescence quenching on the sunny side of the Si. Depending on how long the crack has been present, the size of the quenched area grows, and crack age can be roughly determined. In Fig. 8(d), a presumably “younger” crack compared to the others is marked [48].

EVA fluorescence is even visible in the near IR range and appears in PL images [see Fig. 8(a)]; a darkened rectangular vignette and a quenched EVA signal around cracks are noticeable. Due to these thicker crack lines, cracks get highlighted and are easier to detect than in comparable EL images in Fig. 8(b). We did not encounter any module for which EVA luminescence caused a problem for the Si PL characterization and defect detection.

In EL images, shown for a single cell and different excitation in Fig. 8(b) and (c), no signal from the EVA is visible, because

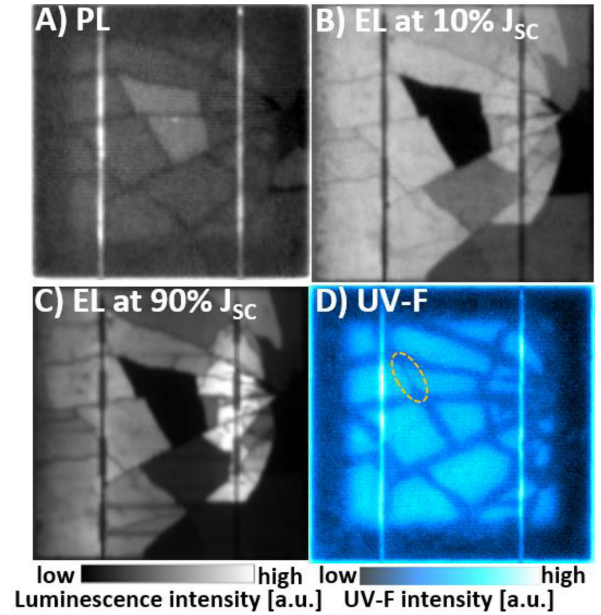


Fig. 8. Magnification of marked cell from images in Fig. 7. (a) PL indoor, (b), EL at  $10\% J_{SC}$ , (c) and at  $90\% J_{SC}$ , and (d) UV-F with a highlighted younger crack.

the emitted photon energy is not high enough to excite EVA. In the PL ratio image, the linear EVA fluorescence signal is not visible due to the nonlinear behavior of Si. Both the IR image and the UV-F image give no information about the crack mode, and thus, no information about inactive areas is obtained.

### C. Interconnection Failures and Snail Trails

Interconnection failures are breakages in the ribbons that connect the Si PV cells. The PV module and magnified PV cell shown in Fig. 9(a) and (b) have two ribbons for each intercell connection. If one of the interconnections breaks, current has to

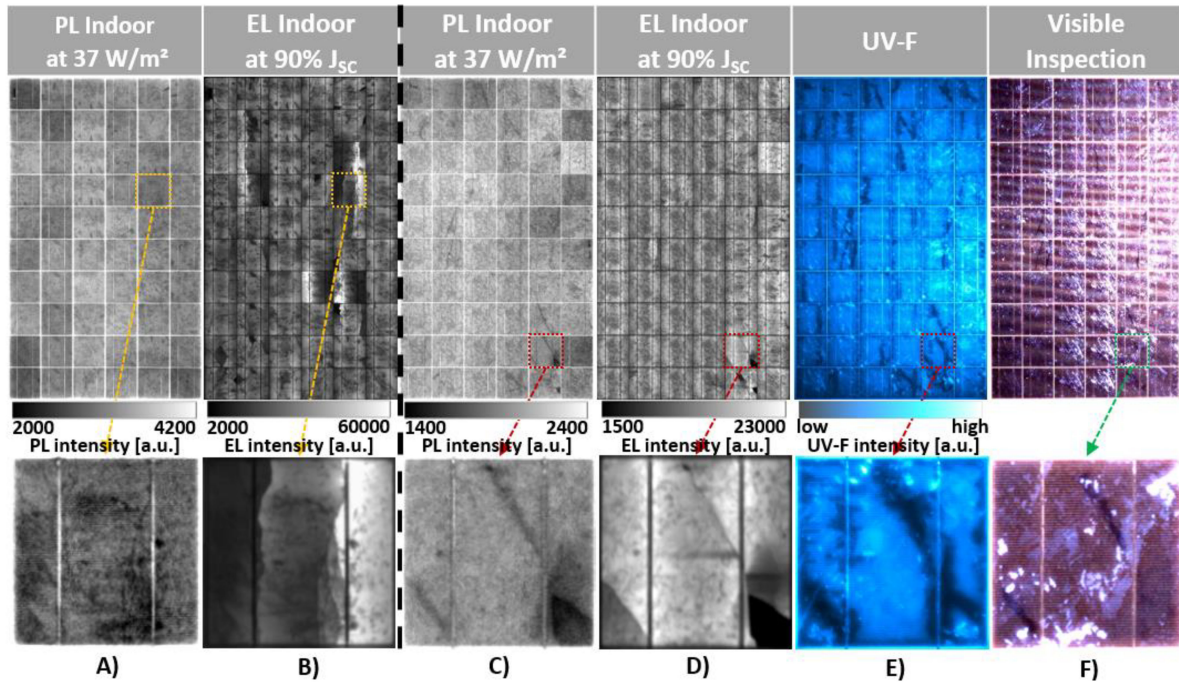


Fig. 9. (a) PL and (b) EL at 90% of  $J_{SC}$  images of one PV module with interconnection failures. (c) PL, (d) EL at 90%  $J_{SC}$ , (e) UV-F, and (f) Visible inspection images of one PV module with visible snail trails and cracks.

be transported over the remaining ribbon, resulting in lateral current transport across the cell. Consequently, an intensity difference between the two cell halves is visible in EL images [see Fig. 9(b)] for high currents and to some extent for low currents. In PL images [see Fig. 9(a)], interconnection failures are not detectable as no current is transported through them. Thermally, interconnection failures are visible depending on cell architecture, the number of broken ribbons, and the irradiance conditions. The lower the percentage of broken ribbons, and the lower the irradiance, the lower is the energy loss of the cells.

Snail trails are the result of corrosion of the metal grid-fingers, induced by water vapor and oxygen diffusing through cracks in Si [53]. Snail trails are visible in visual inspection in the PV module and PV cell images [see Fig. 9(f)]. Water vapor and oxygen diffusion typically also quench EVA fluorescence. Hence, snail trails are visible in UV-F. Anomaly in EVA fluorescence is no indication of snail trails as is apparent from Fig. 7(f) where no snail trails are visible. In PL images [see Fig. 9(c)], snail trails can clearly be recognized, but not in the EL images [see Fig. 9(d)]. Previous reports have found the formation of metal oxide nanoparticles near snail trails in the EVA layer [53], [54]. These particles might quench EVA fluorescence in the NIR region [55] and make snail trails recognizable in PL images.

#### IV. AUTOMATED DEFECT RECOGNITION

Section III shows that PL images are well suited to identify different types of defects on solar cells. Recently, AOI methods have been used to automate the process of on-site and lab-based inspection of solar cells. However, the visibility of defects to human experts in a given modality does not necessarily imply

TABLE I  
RESULTS FROM THE DEFECT CLASSIFICATION EXPERIMENT

		crack	inactive
EL	precision	0.93	0.95
	recall	0.89	0.96
	$F_1$	0.91	0.96
PL	precision	0.92	0.90
	recall	0.89	0.91
	$F_1$	0.91	0.90

detectability by AOI methods. To address this limitation, we conducted an additional experiment comparing the performance of AOI methods for detecting cracks and inactive areas in EL and PL images. This procedure also enabled a quantitative comparison of defect recognition rates for the different luminescence methods.

In a previous work, we investigated the detection and classification of cracks in EL images of solar cells using deep learning [43].

This experiment is a direct continuation of the previous study. We used a ResNet-like architecture in combination with max-pooling, as described in the previous study. We pretrained our model on a dataset consisting of 45 000 labeled EL cell images for classification of cracks and inactive areas. Next, we assemble another dataset consisting of 1200 labeled cells from a different PV module type. Those images are measured with EL and PL. We split the dataset into 600 training and 600 test images for EL and PL and perform fine-tuning for the new PV module type. The model pretrained with the 45 000 EL samples is trained on the 600 EL training images. We repeat the fine-tuning step with

TABLE II  
OVERVIEW AND COMPARISON OF THE DIFFERENT IMAGING TECHNIQUES DEPENDING ON THEIR VISIBILITY OF DIFFERENT DEFECT TYPES

Defect	EL at 90% Jsc	EL at 10% Jsc	PL at 37 W/m <sup>2</sup>	PL ratio	IR	UV-F
PID	depends	visible	visible	visible	visible	invisible
Cracks	visible	visible	visible	visible	invisible	visible
Inactive area	visible	visible	depends	depends	depends	invisible
Bypass diode SC-failures	visible	visible	visible	visible	visible	invisible
Snail trails	depends	invisible	visible	invisible	invisible	depends
EVA degradation	invisible	invisible	visible	invisible	invisible	visible
Interconnection failures	visible	depends	invisible	invisible	depends	invisible

the 600 PL training images. As a result, we obtain two models, one fine-tuned for detecting cracks and inactive areas in our dataset using EL images and the other using PL images. Finally, we analyze the classification performance of both models on the corresponding test set on the detectability of a crack in a cell.

For evaluation, we report classification recall, precision, and  $F_1$ -score. Given the number of true positives (TP) and the number of false negatives (FN), the recall is given by

$$\text{recall} = \frac{\text{TP}}{\text{TP} + \text{FN}}. \quad (4)$$

Furthermore, given the number of TP and false positives (FP), the precision is computed as

$$\text{precision} = \frac{\text{TP}}{\text{TP} + \text{FP}}. \quad (5)$$

$F_1$ -score is computed as the harmonic mean of precision and recall

$$F_1 = 2 \times \frac{\text{precision} \times \text{recall}}{\text{precision} + \text{recall}}. \quad (6)$$

The results of this experiment are summarized in Table I. Automatic classification of cracks is not affected by the choice of PL versus EL images. Both modalities provide robust classification of cracks. For inactive areas, classification with PL performs slightly worse than with EL. This is consistent with the results of our visual study (see Section III) where we concluded that inactive areas are more visible in EL. To be sure that this is not due to a possible bias from pretraining on a large EL dataset, we repeat the experiment without pretraining. This leads to a similar observation, although the models without pretraining perform a little worse. Thus, we show that PL is well suited for automated optical inspection of solar cells with respect to cracks and inactive regions.

## V. CONCLUSION

In this article, we discussed advantages and disadvantages of PL imaging as a possible high throughput outdoor characterization tool for PV plant inspection. We constructed an outdoor-capable PL setup consisting of an excitation unit and a camera, and used this unit to take images of modules with known defects. Images of the same modules were also taken with alternative, state-of-the-art techniques, including EL, IR, and UV-F imaging. For each image, an AOI algorithm was applied for defect detection and analysis. The following seven common defect types were analyzed: PID, cell cracks, inactive areas, defective bypass diodes, snail trails, EVA degradation, and interconnection failures.

Table II summarizes our findings about the detectability of these defects for the various imaging techniques. Out of the selected defects, we were able to identify five with our PL setup: short-circuited bypass diodes, cracks, PID, snail trails, and EVA degradation with a reliable rate, and inactive areas under suitable conditions. Thus, PL enables a combination of Si and encapsulation luminescence characterization with only one high-resolution image and without electrical contact to the PV circuit. Interconnection failure defects are not detectable due to the nature of signal generation in PL.

Five defects could also be detected using EL imaging with at least two excitation currents. Other than in PL, interconnection failures are visible, though snail trails and EVA degradation are not. EL is the most similar technique to PL but, unlike it, is limited by electrical contacting, and is, therefore, less suitable for high throughput measurements.

IR is capable of detecting defects through local energy loss, and can detect deficiencies on cell and module level, but also issues with inverter, or losses caused by shading [56]. Defects on neighboring cells are difficult to separate, though, due to the heat flux within the module. Additionally, in IR, environmental conditions have to be taken into account for interpretation. We show that some defects, cracks, snail trails, and EVA degradation that cannot be found using IR imaging are visible in PL, making this method an interesting complement to IR.

UV-F is capable of detecting cracks and EVA degradation, and its main advantage is the possibility to differentiate cracks by age.

One important factor for inspection methods is throughput. Aerial IR imaging is by far the fastest among our compared inspection methods, where inspection rates up to 1 MW per hour are possible [57]. EL is already used in aerial applications with a throughput of up to 1 MW per night [58], limited by the electrical connection done the previous day at daytime. Handheld EL setups reach throughputs of 16 modules per minute [59]. With our prototype illumination outdoor PL setup in an initial field test, we managed to measure 37 modules in one minute (approx. 0.5 MW per hour), demonstrating the capability of the method to work in a high throughput mode. Currently, a stationary power supply connected by cable is used with our PL setup. This connection limits the area for measurable PV systems and unthreading the cable reduces throughput. A battery power supply, currently under development, will be used to address the issue and we expect it to increase throughput.

The most important factor for choosing the right characterization method is how fast data is evaluated and how precise suitable countermeasures for the defects are determined. Complementary methods might be used to get a more profound defect analysis. Defect visibility shown in Table II can be used to choose the right technique or techniques. A high coverage might be achieved, for example, for IR and PL and defects from PID, cracks, inactive areas, polymer defects, and interconnection failure are detectable with their severity, fully without any electrical connection.

In this early stage of development for an outdoor PL setup, improvements remain necessary. For example, the excitation intensity can be increased to reduce integration time. In addition, the integration of PL imaging in drones is an interesting perspective. Algorithms, which are already available for EL to automate and improve data analysis, need to be developed or adapted. Despite this low level of maturity, we could already demonstrate that PL is not only complementary, but also quite powerful in comparison to various well-established methods for optical inspection of PV modules.

#### ACKNOWLEDGMENT

The authors would like to thank the Allianz Risk Consulting GmbH/Allianz Zentrum für Technik (AZT) in Munich, Germany, and Rauschert Heinersdorf-Pressig GmbH for supporting the project with a large number of PV modules.

#### REFERENCES

- [1] J. A. Tsanakas, L. Ha, and C. Buerhop, "Faults and infrared thermographic diagnosis in operating c-Si photovoltaic modules: A review of research and future challenges," *Renewable Sustain. Energy Rev.*, vol. 62, pp. 695–709, Sep. 2016.
- [2] IEC, "Photovoltaic (PV) systems—Requirements for testing, documentation and maintenance—Part 3: Photovoltaic modules and plants—outdoor infrared thermography," IEC, Paris, France, Tech. Rep. IEC TS 62446-3:2017, 2017.
- [3] C. Camus *et al.*, "Site-specific assessment of mechanical loads on photovoltaic modules from meteorological reanalysis data," *Sol. Energy*, vol. 188, pp. 1134–1145, Aug. 2019.
- [4] Solar Power Europe (SPE), *Global Market Outlook for Solar Power: 2019–2023*, Solar Power Europe (SPE), Brussels, Belgium, 2019.
- [5] Arbeitsgruppe Erneuerbare Energien-Statistik (AGEE-Stat), "Zeitreihen zur entwicklung der erneuerbaren energien in deutschland," Umweltbundesamt (UBA), Dessau-Roßlau, Germany, 2020.
- [6] C. Buerhop, T. Pickel, H. Scheuerpflug, C. Camus, J. Hauch, and C. J. Brabec, "Statistical overview of findings by IR-inspections of PV-plants," *Proc. SPIE*, vol. 9938, Sep. 2016, Art. no. 99380L.
- [7] U. Jahn *et al.*, "Review on infrared (IR) and electroluminescence (EL) imaging for photovoltaic field applications," IEA, Paris, France, Rep. IEA-PVPS T13-10:2018, 2018.
- [8] U. Hoyer *et al.*, "Analysis of PV modules by electroluminescence and IR thermography," in *Proc. 24th Eur. Photovolt. Sol. Energy Conf.*, 2009, pp. 21–25.
- [9] C. Buerhop and H. Scheuerpflug, "Characterization of defects in PV-Modules by their temperature development using IR- Thermography," in *Proc. 31st Eur. Photovolt. Sol. Energy Conf. Exhib.*, 2015, pp. 1789–1792.
- [10] W. Mühlleisen *et al.*, "Scientific and economic comparison of outdoor characterisation methods for photovoltaic power plants," *Renewable Energy*, vol. 134, pp. 321–329, Apr. 2019.
- [11] C. Buerhop *et al.*, "IR-images of PV-modules with potential induced degradation (PID) correlated to monitored string power output," *Proc. SPIE*, vol. 9938, 2016, Art. no. 99380J.
- [12] M. Köntges *et al.*, "Review of failures of photovoltaic modules," IEA, Paris, France, Report IEA-PVPS T13-01:2014, 2014.
- [13] R. Ebner *et al.*, "Optical characterization of different thin film module technologies," *Int. J. Photoenergy*, vol. 2015, pp. 1–12, 2015.
- [14] J. Haunschild *et al.*, "Review of tools and approaches for inline quality control in high efficiency silicon solar cell production," in *Proc. 33rd Eur. PV Sol. Energy Conf. Exhib.*, 2017, pp. 870–874.
- [15] A. A. R. M. A. Ebayeh and A. Mousavi, "A review and analysis of automatic optical inspection and quality monitoring methods in electronics industry," *IEEE Access*, vol. 8, pp. 183192–183271, 2020.
- [16] D. Stromer, A. Vetter, H. C. Oezkan, C. Probst, and A. Maier, "Enhanced crack segmentation (eCS): A reference algorithm for segmenting cracks in multicrystalline silicon solar cells," *IEEE J. Photovolt.*, vol. 9, no. 3, pp. 752–758, May 2019.
- [17] Y. Zhao, K. Zhan, Z. Wang, and W. Shen, "Deep learning-based automatic detection of multitype defects in photovoltaic modules and application in real production line," *Prog. Photovolt. Res. Appl.*, vol. 29, no. 4, pp. 471–484, Apr. 2021.
- [18] Y. Chiou, J. Liu, and Y. Liang, "Micro crack detection of multi-crystalline silicon solar wafer using machine vision techniques," *Sens. Rev.*, vol. 31, no. 2, pp. 154–165, Mar. 2011.
- [19] T. Fuyuki, H. Kondo, T. Yamazaki, Y. Takahashi, and Y. Uraoka, "Photographic surveying of minority carrier diffusion length in polycrystalline silicon solar cells by electroluminescence," *Appl. Phys. Lett.*, vol. 86, no. 26, pp. 1–3, 2005.
- [20] IEC, "Photovoltaic devices—Part 13: Electroluminescence of photovoltaic modules," IEC, Paris, France Tech. Rep. IEC TS 60904-13:2018, 2018.
- [21] T. Kropp, M. Schubert, and J. Werner, "Quantitative prediction of power loss for damaged photovoltaic modules using electroluminescence," *Energies*, vol. 11, no. 5, May 2018, Art. no. 1172.
- [22] B. Doll *et al.*, "Contactless outdoor photoluminescence of silicon photovoltaic modules with large area excitation source," in *Proc. 37th Eur. Photovolt. Sol. Energy Conf. Exhib.*, 2020, pp. 1370–1373.
- [23] Y. Zhu, M. K. Juhl, T. Trupke, and Z. Hameiri, "Photoluminescence imaging of silicon wafers and solar cells with spatially inhomogeneous illumination," *IEEE J. Photovolt.*, vol. 7, no. 4, pp. 1087–1091, Jul. 2017.
- [24] T. Trupke *et al.*, "Photoluminescence imaging for photovoltaic applications," *Energy Procedia*, vol. 15, no. 2011, pp. 135–146, 2012.
- [25] I. Zafirovska, M. K. Juhl, and T. Trupke, "Comparison of line scan luminescence imaging techniques for defect characterisation in crystalline silicon solar modules," in *Proc. IEEE 7th World Conf. Photovolt. Energy Convers. (Joint Conf. 45th IEEE PVSC, 28th PVSEC 34th EU PVSEC)*, Jun. 2018, pp. 1364–1369.
- [26] G. A. dos R. Benatto *et al.*, "Photoluminescence imaging induced by laser line scan: Study for outdoor field inspections," in *Proc. IEEE 7th World Conf. Photovolt. Energy Convers. (Joint Conf. 45th IEEE PVSC, 28th PVSEC 34th EU PVSEC)*, Jun. 2018, pp. 0395–0399.
- [27] J. Adams *et al.*, "Non-Stationary outdoor EL-Measurements with a fast and highly sensitive ingaas camera," in *Proc. 32nd Eur. Photovolt. Sol. Energy Conf. Exhib.*, Jun. 2016, pp. 1837–1841.

- [28] I. Zafirovska, M. K. Juhl, and T. Trupke, "Comparison of line scan luminescence imaging techniques for defect characterisation in crystalline silicon solar modules," in *Proc. IEEE 7th World Conf. Photovolt. Energy Convers. (Joint Conf. 45th IEEE PVSC, 28th PVSEC 34th EU PVSEC)*, Jun. 2018, pp. 1364–1369.
- [29] G. Rey, T. Nagle, and T. Trupke, "Line scanning photoluminescence imaging to study the effects of heat stress in thin-film modules," in *Proc. 47th IEEE Photovoltaic Specialists Conf.*, 2020, pp. 0384–0388.
- [30] A. Gisele *et al.*, "Detection of solar cell cracks by laser line induced lateral currents," in *Proc. 37th Eur. Photovolt. Sol. Energy Conf. Exhib.*, 2020, pp. 1053–1057.
- [31] I. Zafirovska, M. K. Juhl, J. W. Weber, O. Kunz, and T. Trupke, "Module inspection using line scanning photoluminescence imaging," in *Proc. 32nd Eur. Photovolt. Sol. Energy Conf. Exhib.*, 2016, pp. 1826–1829.
- [32] R. Bhoopathy, O. Kunz, M. Juhl, T. Trupke, and Z. Hameiri, "Outdoor photoluminescence imaging of photovoltaic modules with sunlight excitation," *Prog. Photovolt. Res. Appl.*, vol. 26, no. 1, pp. 69–73, Jan. 2018.
- [33] R. Bhoopathy, O. Kunz, M. Juhl, T. Trupke, and Z. Hameiri, "Outdoor photoluminescence imaging of solar panels by contactless switching: Technical considerations and applications," *Prog. Photovolt. Res. Appl.*, vol. 28, no. 3, pp. 217–228, Mar. 2020.
- [34] L. Stoicescu, M. Reuter, and J. H. Werner, "Daysy: Luminescence imaging of PV modules in daylight," in *Proc. 29th Eur. Photovolt. Sol. Energy Conf. Exhib.*, 2014, pp. 2553–2554.
- [35] B. Doll *et al.*, "Quantitative assessment of the influence of camera and parameter choice for outdoor electroluminescence investigations of silicon photovoltaic panels," *Zeitschrift für Naturforsch. A*, vol. 74, no. 8, pp. 645–653, Aug. 2019.
- [36] M. D. Abbott *et al.*, "Application of photoluminescence characterization to the development and manufacturing of high-efficiency silicon solar cells," *J. Appl. Phys.*, vol. 100, no. 11, 2006, Art. no. 114514.
- [37] D. C. Jordan *et al.*, "High efficiency module degradation—From atoms to systems," in *Proc. 37th Eur. Photovolt. Sol. Energy Conf. Exhib.*, 2020, pp. 828–833.
- [38] T. Trupke, R. A. Bardos, and M. D. Abbott, "Self-consistent calibration of photoluminescence and photoconductance lifetime measurements," *Appl. Phys. Lett.*, vol. 87, no. 18, pp. 1–3, 2005.
- [39] J. Haunschmid, M. Glatthaar, M. Kasemann, S. Rein, and E. R. Weber, "Fast series resistance imaging for silicon solar cells using electroluminescence," *Phys. Status Solidi - Rapid Res. Lett.*, vol. 3, no. 7/8, pp. 227–229, Oct. 2009.
- [40] S. Spataru *et al.*, "Quantifying solar cell cracks in photovoltaic modules by electroluminescence imaging," in *Proc. IEEE 42nd Photovoltaic Specialist Conf.*, Jun. 2015, pp. 1–6.
- [41] J. M. Greulich *et al.*, "Comparison of inline crack detection systems for multicrystalline silicon solar cells," *IEEE J. Photovolt.*, vol. 10, no. 5, pp. 1389–1395, Sep. 2020.
- [42] M. Hoffmann *et al.*, "Deep Learning-based pipeline for module power prediction from EL measurements," *Prog. Photovolt. Res. Appl.*, vol. 29, pp. 920–935, 2021. [Online]. Available: <https://doi.org/10.1002/pip.3416>.
- [43] M. Mayr, M. Hoffmann, A. Maier, and V. Christlein, "Weakly supervised segmentation of cracks on solar cells using normalized LP norm," in *Proc. IEEE Int. Conf. Image Process.*, 2019, pp. 1885–1889.
- [44] J. Teubner *et al.*, "Quantitative assessment of the power loss of silicon PV modules by IR thermography and its dependence on data-filtering criteria," *Prog. Photovolt. Res. Appl.*, vol. 27, no. 10, pp. 856–868, Oct. 2019.
- [45] L. Bommes *et al.*, "Pipeline for detection, mapping and fault classification of modules in IR videos of PV plants," *Prog. Photovolt.*, 2021, pp. 1–16. [Online]. Available: <https://doi.org/10.1002/pip.3448>
- [46] D. L. King, M. A. Quintana, J. A. Kratochvil, D. E. Ellibee, and B. R. Hansen, "Photovoltaic module performance and durability following long-term field exposure," *Prog. Photovolt. Res. Appl.*, vol. 8, no. 2, pp. 241–256, Mar. 2000.
- [47] I. K. M. Köntges and S. Kajari-Schröder, "Cell cracks measured by UV fluorescence in the field," in *Proc. 27th Eur. Photovolt. Sol. Energy Conf. Exhib.*, 2012, pp. 3033–3040.
- [48] M. Köntges, S. Kajari-Schröder, and I. Kunze, "Crack statistic for wafer-based silicon solar cell modules in the field measured by UV fluorescence," *IEEE J. Photovolt.*, vol. 3, no. 1, pp. 95–101, Jan. 2013.
- [49] A. Morlier, M. Siebert, I. Kunze, G. Mathiak, and M. Kontges, "Detecting photovoltaic module failures in the field during daytime with ultraviolet fluorescence module inspection," *IEEE J. Photovolt.*, vol. 7, no. 6, pp. 1710–1716, Nov. 2017.
- [50] B. Gilleland, W. B. Hobbs, and J. B. Richardson, "High throughput detection of cracks and other faults in solar PV modules using a high-power ultraviolet fluorescence imaging system," in *Proc. IEEE 46th Photovoltaic Specialists Conf.*, Jun. 2019, pp. 2575–2582.
- [51] S. Pingel *et al.*, "Potential induced degradation of solar cells and panels," in *Proc. 35th IEEE Photovoltaic Specialists Conf.*, Jun. 2010, pp. 002817–002822.
- [52] D. Lausch *et al.*, "Potential-Induced degradation (PID): Introduction of a novel test approach and explanation of increased depletion region recombination," *IEEE J. Photovolt.*, vol. 4, no. 3, pp. 834–840, May 2014.
- [53] S. Richter, M. Werner, S. Swatek, and C. Hagendorf, "Understanding the snail trail effect in silicon solar modules on microstructural scale," in *Proc. 27th Eur. Photovolt. Sol. Energy Conf. Exhib.*, 2012, pp. 3439–3441.
- [54] I. Duerr, J. Bierbaum, J. Metzger, J. Richter, and D. Philipp, "Silver grid finger corrosion on snail track affected PV modules—Investigation on degradation products and mechanisms," *Energy Procedia*, vol. 98, pp. 74–85, Nov. 2016.
- [55] Y. Delgado-Beleno, C. E. Martinez-Nuñez, M. Cortez-Valadez, N. S. Flores-López, and M. Flores-Acosta, "Optical properties of silver, silver sulfide and silver selenide nanoparticles and antibacterial applications," *Mater. Res. Bull.*, vol. 99, pp. 385–392, Mar. 2018.
- [56] S. Gallardo-Saavedra *et al.*, "Nondestructive characterization of solar PV cells defects by means of electroluminescence, infrared thermography, I–V curves and visual tests: Experimental study and comparison," *Energy*, vol. 205, Aug. 2020, Art. no. 117930.
- [57] A. K. V. de Oliveira, M. Aghaei, U. E. Madukanya, L. Nascimento, and R. Ruther, "Aerial infrared thermography of a utility-scale PV plant after a meteorological tsunami in Brazil," in *Proc. IEEE 7th World Conf. Photovolt. Energy Convers. (Joint Conf. 45th IEEE PVSC, 28th PVSEC 34th EU PVSEC)*, Jun. 2018, pp. 0684–0689.
- [58] S. Koch, T. Weber, C. Sobottka, A. Fladung, and P. Clemens, "Outdoor electroluminescence imaging of crystalline photovoltaic modules: Comparative study between manual ground-level inspections and drone-based aerial surveys," in *Proc. 32nd Eur. Photovolt. Sol. Energy Conf. Exhib.*, 2016, pp. 1736–1740.
- [59] B. Doll *et al.*, "High-throughput, outdoor characterization of photovoltaic modules by moving electroluminescence measurements," *Opt. Eng.*, vol. 58, no. 8, pp. 1–13, Aug. 2019.